CHAPTER 5:
Point Spread Function

In This Chapter...

Effects of OTA Spherical Aberration / 85
Aberration Correction / 86
Wavefront Quality / 90
CCD Pixel Response Function / 91
Model PSFs / 92
PSF Variations with Field Position / 95
PSF Variations with Time / 97
Large Angle Scattering / 99
Ghost Images / 100
Optical Distortion / 103

5.1 Effects of OTA Spherical Aberration

The OTA spherical aberration produces a Point Spread Function (PSF—the apparent surface brightness profile of a point source), as presented to the instruments, with broad wings. Briefly, the fraction of the light within the central 0.1″ was reduced by a factor of about 5. The resulting PSF had "wings" which extended to large radii (several arcseconds), greatly reducing the contrast of the images and degrading the measurements of sources near bright objects or in crowded fields. Burrows et al. (1991, Ap. J. Lett. 369, L21) provide a more complete description of the aberrated HST PSF. Figure 5.1 shows the PSF in three cases. It shows the aberrated HST PSF, the WFPC2 PSF, and for comparison the PSF that would be obtained from a long integration if HST were installed at a ground based observatory with one arcsecond seeing. All of the PSFs were computed at 4000Å. The FWHM of the image both before and after the installation of WFPC2 is approximately proportional to wavelength, at least before detector resolution and MTF effects are considered. (The WF/PC-1 core was approximately 50% broader than the core that is obtained with WFPC2). Figure 5.2 shows the encircled energy (EE), the proportion of the total energy from a point source within a given radius of the image center, for the same three

Figure 5.1: PSF Surface Brightness. The percentage of the total flux at 4000Å falling on a PC pixel as a function of the distance from the peak of a star image.

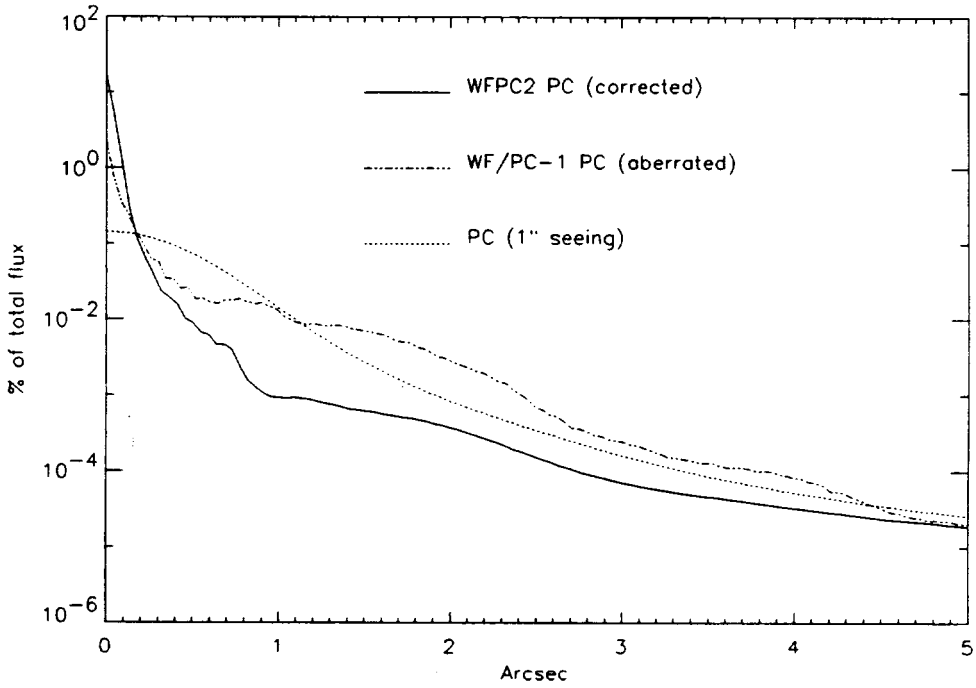

cases. The WFPC2 curve shown is the average of measurements taken with F336W and F439W. It can be seen that the core of the image in WFPC2 contains most of the light. At this wavelength, 65% of the light is contained within a circle of radius 0.1″. However, this proportion is considerably less than the optics deliver. The reason for this is discussed in the Section 5.4. Encircled energy curves for other filters are shown in Figures 5.3 and 5.4; note that these curves are normalized to unity at 1.0″ radius.

5.2 Aberration Correction

WFPC2 has corrective figures on the relay secondary mirrors where the primary mirror is imaged; this optical correction recovers near-diffraction limited images over the entire CCD fields-of-view. Proper correction requires tight optical alignment tolerances, which are facilitated on-orbit by actuated optics. The corrective optics enable essentially all of the scientific objectives of the original WF/PC-1 to be met.

Figure 5.2: Encircled Energy. The percentage of the total flux at 4000Å within a given radius of the image peak.

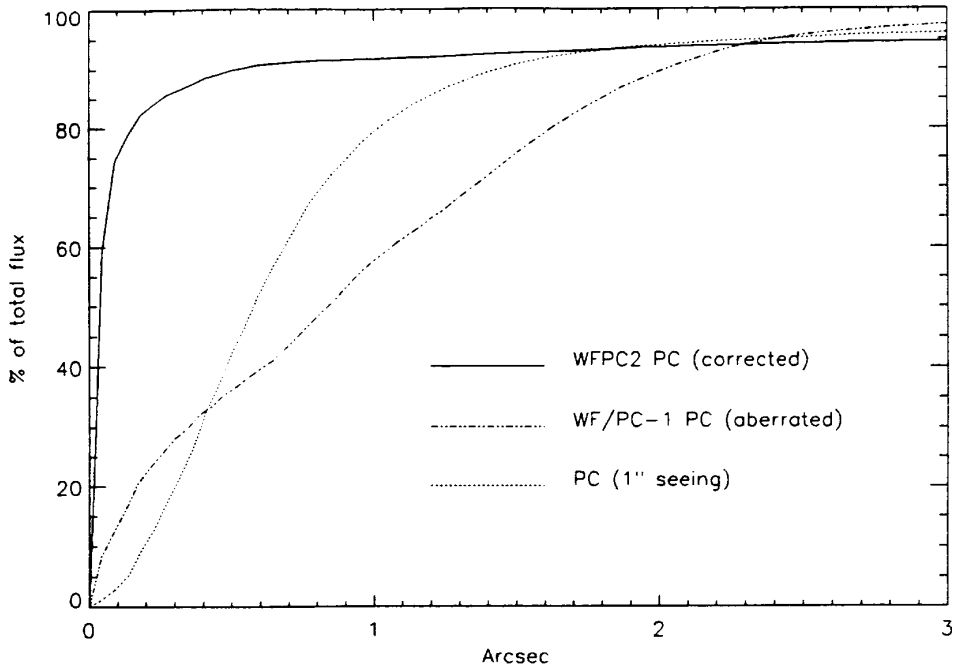

Table 5.1: Wavefront Error Budget.

Camera	WFC (F/12.9)	PC(F/28.3)
Design error	λ/143	λ/50
Fabrication and alignment error	λ/14.7	λ/14.7
Alignment stability error	λ/25	λ/25
Total wavefront error	λ/12.6	λ/12.3

Through a number of independent analyses, based on investigations of star images obtained on-orbit, and the examination of fixtures used during the figuring of the primary mirror, the aberrations of the HST optics were accurately characterized. The primary mirror was figured to an incorrect conic constant: –1.0139±0.005 rather than the –1.0023 design requirement, resulting in a large amount of spherical aberration. The optical design of WFPC2 creates an image of the OTA primary mirror near the surface of the relay Cassegrain secondary mirror in each of its channels. This design minimizes vignetting in the relay optics, but more importantly, facilitates correction of spherical aberration in the OTA primary by application of the same error (but with opposite sign) to the relay secondary. The optical figure of the WFPC2 secondary mirrors contains a compensating

Figure 5.3: Encircled Energy for CCD PC1. The fraction of energy encircled is plotted vs. aperture radius for several filters. Curves are normalized to unity at a radius of 1.0″. From Holtzman, et al., 1995a.

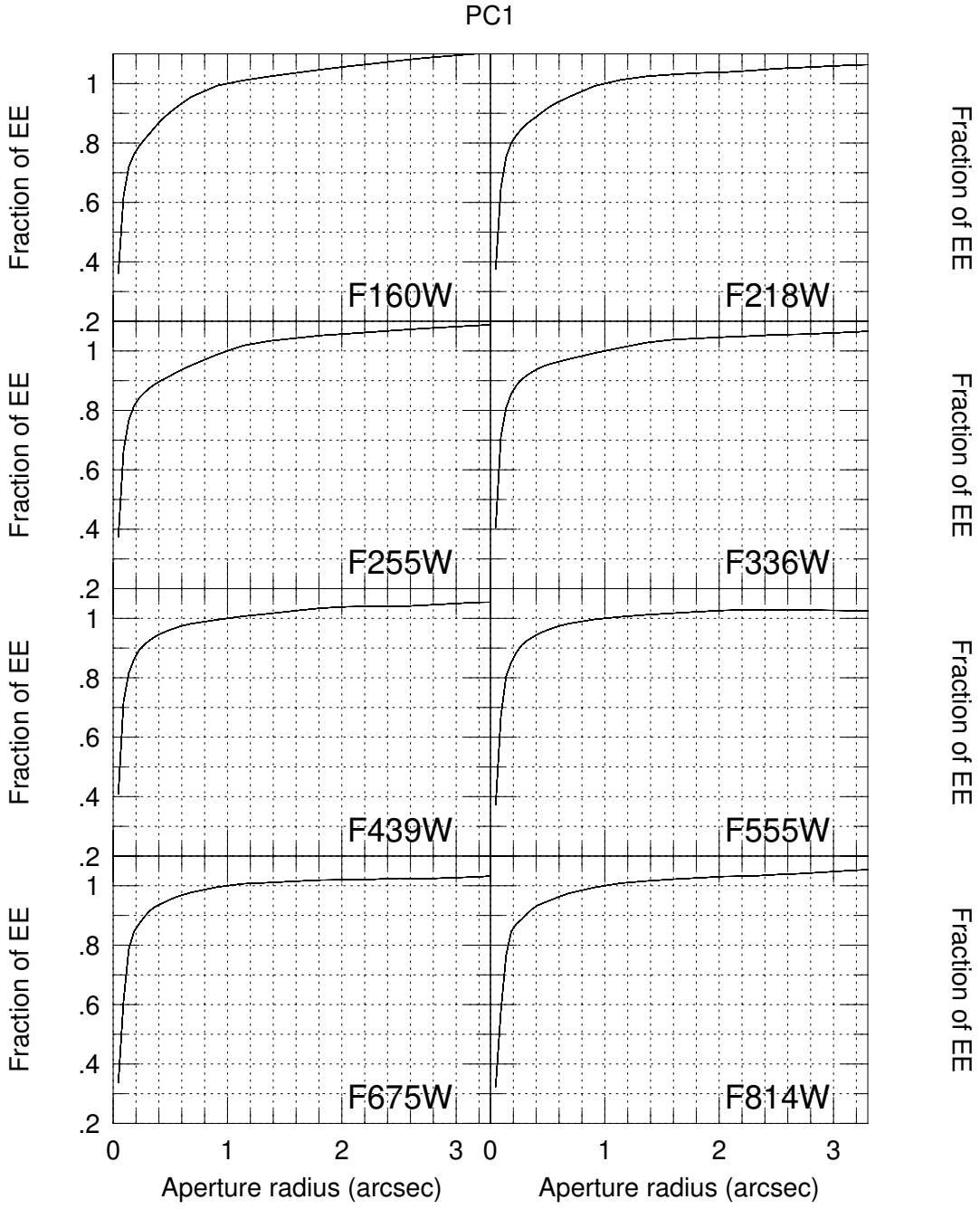

Figure 5.4: Encircled Energy for CCD WF3. The fraction of energy encircled is plotted vs. aperture radius for several filters. Curves are normalized to unity at a radius of 1.0″. From Holtzman, et al., 1995a.

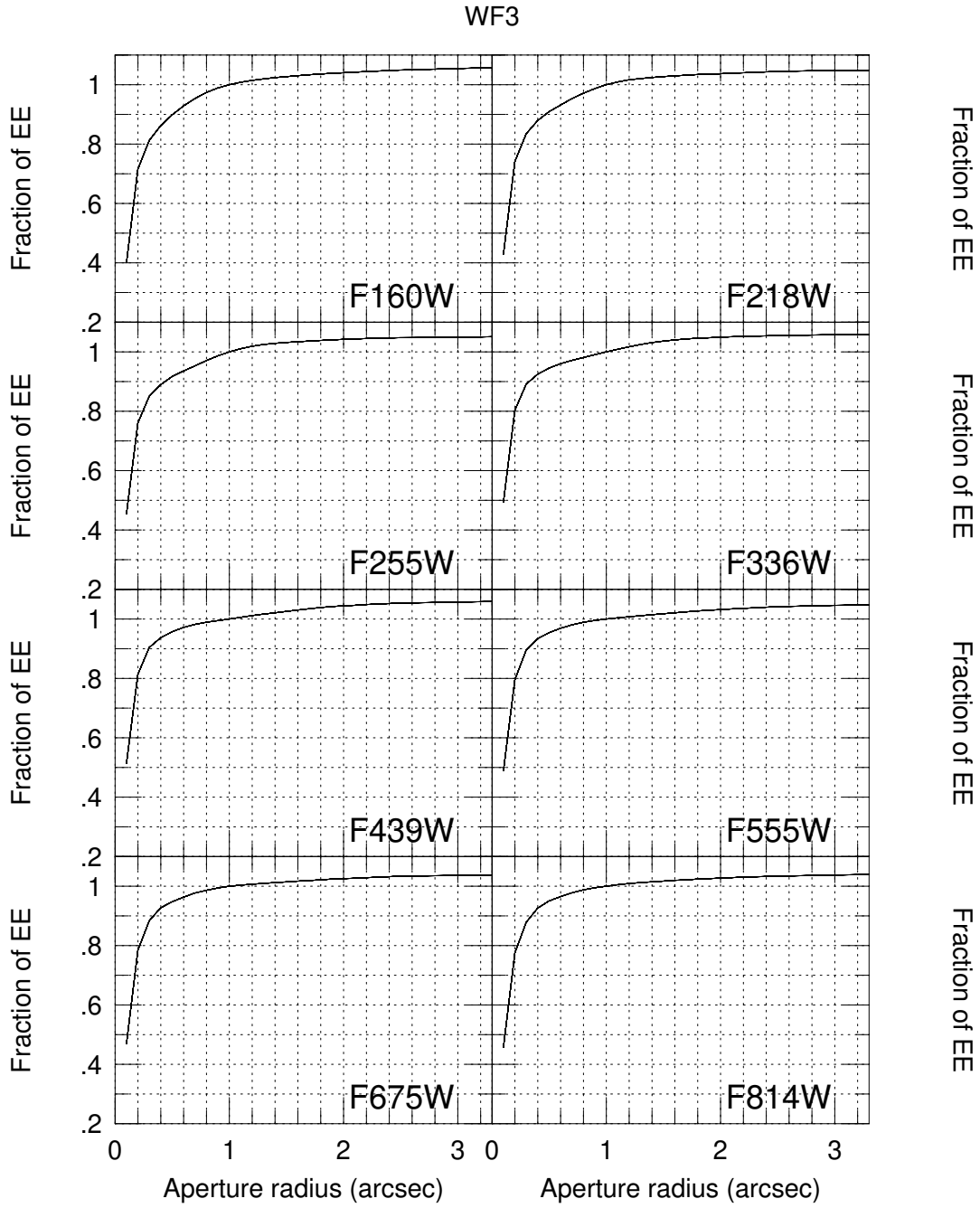

"error" in the conic constant. By adopting a prescription within the error bars for the HST primary mirror, corrective secondary mirrors were made with sufficient accuracy that the residual spherical aberration in the WFPC2 wavefront is small compared to other terms in the WFPC2 optical wavefront budget.

On the other hand, new and stringent alignment requirements were created by the steep optical figure on the corrective relay secondary mirrors. The primary mirror image must be accurately centered on the corrective mirror, and must have the correct magnification. Centering is the most demanding requirement. A failure to center accurately would create a new aberration in the form of coma. A misalignment of 7% of the pupil diameter introduces as much RMS wavefront error as was present in the form of spherical aberration prior to the introduction of corrective optics. The new requirements for alignment accuracy and stability led to the introduction of a tip-tilt mechanism on the pick-off mirror, to compensate for camera alignment uncertainties with respect to the OTA, and actuated fold mirrors which can compensate for internal misalignments. There was an additional term in the CEIS specification of the overall instrument wavefront error budget for alignment stability. It is $\lambda/25$ RMS at 6328Å, as shown in Table 5.1.

"Design error" refers to the aberrations inherent in the design itself, which would be seen if the optics conformed perfectly to their specifications. All of the optics were fabricated and integrated into the WFPC2 optical bench. It was established on the basis of component tests, end-to-end optical interferometry, and through focus phase retrieval, that the WFPC2 optical system performed within the stated tolerances for "fabrication and alignment" in the laboratory environment. What remained was to demonstrate the stability of the optical alignment after launch vibration and in response to the thermal environment on-orbit. The "stability" line anticipated these uncertainties, and has been verified during early science operations.

5.3 Wavefront Quality

The conclusion of the extensive optical testing in thermal vacuum was that the cameras are well corrected to within the specifications. The measured wavefront errors in the four cameras were 1/30, 1/17, 1/40, and 1/21 waves at 6328Å. The dominant problem was a small difference in focus between the four cameras. The actuated fold mirrors and pick-off mirror mechanism performed flawlessly in correcting residual coma aberrations in the image, and enabled the on-orbit alignment procedures. By defocusing the OTA secondary mirror, a very accurate alignment of the cameras was accomplished. A side effect was that the aberrations in each camera were measured (Krist and Burrows, Applied Optics, 1995). The results are given in Table 5.2. These values were used in generating the simulated PSFs given in section 5.5, "Model PSFs", on page 92.

Table 5.2: Aberrations in Each Camera. The numbers quoted are RMS wavefront errors in microns over the HST aperture (Zernike coefficients).

	Aberration	PC1	WF2	WF3	WF4
Z4	Defocus	0.0000	0.0410	0.0640	0.0480
Z5	0˚ Astig	0.0229	0.0109	0.0126	0.0163
Z6	45˚ Astig	0.0105	0.0041	0.0113	0.0190
Z7	V2 Coma	0.0000	0.0012	-0.0037	-0.0090
Z8	V3 Coma	-0.0082	0.0061	-0.0100	0.0019
Z9	X Clover	0.0063	0.0121	0.0010	0.0096
Z10	Y Clover	0.0023	0.0091	0.0130	0.0042
Z11	Spherical	-0.0131	-0.0215	-0.0265	-0.0247
Z22	5th Spherical	0.0034	0.0034	0.0036	0.0029
	Zonal Errors	0.0180	0.0180	0.0180	0.0180
	Total (RS5)	0.0353	0.0537	0.0755	0.0637
	Budget	0.0813	0.0794	0.0794	0.0794

5.4 CCD Pixel Response Function

From Thermal Vacuum testing, there was evidence that the images are not as sharp as expected, despite the good wavefront quality. The decrease in sharpness corresponds to a loss in limiting magnitude of about 0.5 magnitudes in the WF cameras, and less in the PC.

Further testing, by covering a flight spare CCD with a 2µm pinhole grid in an opaque metallic mask and illuminating it with a flat field source, showed that even when a pinhole was centered over a pixel only about 70% of the light was detected in that pixel.

For practical purposes, the effect can be modeled as equivalent to about 40 mas RMS gaussian jitter in the WFC, and 18 mas in the PC (as compared with the typical real pointing jitter of ~3 mas delivered by the excellent HST pointing control system). Alternatively, at least in the V band, it can be modeled by convolving a simulated image by the following kernel, which gives the pixel response function averaged within pixels:

$$K = \begin{bmatrix} 0.016 & 0.067 & 0.016 \\ 0.080 & 0.635 & 0.080 \\ 0.015 & 0.078 & 0.015 \end{bmatrix}$$

One clue is the wavelength dependence of the observed sharpness: the results from the 2μm pinhole grid test get worse at longer wavelengths. This may reflect the greater penetration into the silicon of low energy photons, which facilitates the diffusion of photoelectrons across the pixel boundaries defined by the frontside gate structure.

There is also evidence for sub-pixel QE variations at the 10% level. There is an implied dependence on pixel phase for stellar photometry. This has been seen at about the 1% level in on-orbit data. The work of Jorden, Deltorn, and Oates (Greenwich Observatory Newsletter 9/93) has yielded quite similar results, and suggests that sub-pixel response must be taken into account when seeking to understand the behavior of all CCD detectors forming undersampled images.

5.5 Model PSFs

Considerable effort has gone into the modeling of the HST point spread function (PSF), both in order to measure the optical aberrations in support of the WFPC2, COSTAR, and advanced scientific instruments, and to provide PSFs for image deconvolution in the aberrated telescope. Such PSFs are noise free and do not require valuable HST observing time. Software to generate model PSFs for any filter and at any location within the field-of-view is available from the STScI (TIM package, Hasan and Burrows 1993; TinyTIM package, Krist 1995). The results are illustrated in Tables 5.3 and 5.4 for the PC1 and WF2 cameras, respectively. A representative PSF is on the left in each panel. It meets the wavefront error budget, with the measured mix of focus, coma, astigmatism, and spherical aberration. It has been degraded by the pixel response function as discussed in the Section 5.4. On the right is the diffraction limited case for comparison. In each case the percentage of the total flux in a central 5x5 pixel region of a point source is displayed. The peak of the star image can be at an arbitrary point relative to the boundaries of the CCD pixels. Two cases are shown: one where the star is approximately centered on a pixel, and one where it is approximately centered at a pixel corner. As a consequence of the under-sampling in the WFPC2, the limiting magnitude attainable in the background limit varies by about 0.5 magnitude, depending on the position of the source within the CCD pixel. This point is discussed in more detail in Chapter 6.

Neither observed nor modeled PSFs will provide a perfect match to the PSF in actual science observations, due to modeling uncertainties, the “jitter” in the HST pointing, and orbit to orbit variations in telescope focus (“breathing”—which seems to be generally limited to about 1/20 wave peak-to-peak). Jitter is not predictable but can be recovered to a reasonable extent for observations obtained in Fine Lock. In long exposures, up to about 10 mas of apparent pointing drift may occur as a result of the breathing effects in the FGS, although smaller variations of ~3 mas are typical.

Table 5.3: PC Point Spread Functions. Shown as percentages (out of 100 percent) of the total flux in a 5 by 5 pixel region. On the left in each case is a model PSF with the observed wavefront errors and pixel response function. On the right is the diffraction limited case for comparison.

WFPC2 Model PSF				2000 Å: Peak near corner of PC pixel			Diffraction Limited PSF		
0.9	2.3	2.3	0.9	0.3	0.2	0.6	0.5	0.3	0.1
2.5	10.3	12.7	2.5	0.5	0.6	17.6	20.9	0.5	0.1
1.9	11.2	13.3	2.6	0.5	0.5	20.9	26.0	0.6	0.2
0.9	2.1	2.7	1.4	0.3	0.3	0.5	0.6	0.3	0.1
0.3	0.5	0.5	0.4	0.2	0.1	0.1	0.2	0.1	0.2
				Peak near center of pixel					
0.3	0.7	1.3	0.8	0.5	0.1	0.3	0.4	0.2	0.2
0.7	2.6	6.4	3.2	0.8	0.3	0.6	4.9	0.6	0.3
1.2	6.3	25.0	6.9	1.4	0.4	4.9	62.9	6.3	0.4
0.6	2.2	5.9	3.6	0.9	0.3	0.5	6.3	0.7	0.4
0.4	0.8	1.4	1.1	0.4	0.2	0.3	0.4	0.4	0.2
				4000 Å: Peak near corner of PC pixel					
0.9	2.5	3.5	1.2	0.2	0.3	2.5	2.5	0.3	0.1
3.6	10.8	12.0	3.1	0.4	2.5	14.3	15.8	2.7	0.2
2.7	11.5	12.9	3.5	0.4	2.5	15.8	17.6	3.0	0.2
0.8	3.0	3.4	1.3	0.3	0.3	2.7	3.0	0.4	0.1
0.2	0.4	0.4	0.3	0.2	0.1	0.2	0.2	0.1	0.1
				Peak near center of pixel					
0.3	0.6	0.8	0.9	0.3	0.1	0.2	0.3	0.2	0.1
0.9	4.0	6.6	4.9	0.8	0.2	3.8	4.4	3.8	0.2
0.9	6.9	26.1	7.0	0.8	0.3	4.5	49.4	5.1	0.4
0.5	3.4	6.8	4.9	0.9	0.2	3.8	5.0	4.3	0.2
0.2	0.6	0.8	0.9	0.4	0.1	0.2	0.4	0.2	0.1
				6000 Å: Peak near corner of PC pixel					
2.0	2.6	3.4	2.4	0.5	2.1	2.3	2.0	2.1	0.2
3.4	9.8	10.4	2.9	0.6	2.2	11.4	12.8	2.1	0.6
2.8	10.6	11.2	3.2	0.6	2.0	12.9	14.1	2.1	0.6
1.6	2.8	3.1	2.4	0.5	2.0	2.0	2.1	2.3	0.2
0.4	0.6	0.7	0.5	0.2	0.2	0.5	0.6	0.2	0.1
				Peak near center of pixel					
0.5	1.2	1.7	1.7	0.6	0.2	1.5	1.8	1.4	0.3
1.7	3.1	5.9	3.6	1.6	1.5	2.4	4.3	2.2	1.6
2.0	6.0	20.7	6.6	1.8	I.8	4.4	31.6	5.3	2.0
1.2	2.9	6.2	3.7	1.7	1.4	2.1	5.4	2.3	1.7
0.4	1.3	2.0	1.7	0.6	0.2	1.5	1.9	1.7	0.3
				8000 Å: Peak near corner of PC pixel					
1.6	1.9	2.2	1.9	1.1	1.8	0.9	0.9	1.5	1.1
2.1	9.3	9.7	2.1	1.1	0.9	11.7	12.6	1.0	1.4
2.0	9.8	10.1	2.4	1.1	0.9	12.6	13.3	1.0	1.5
1.4	2.1	2.1	1.8	1.1	1.5	1.0	1.0	1.6	1.2
0.8	1.2	1.3	1.1	0.4	1.1	1.4	1.5	1.2	0.2
				Peak near center of pixel					
1.2	1.4	1.5	1.8	1.4	1.3	1.8	1.1	1.6	1.4
I.8	2.5	6.0	2.8	I.6	I.8	1.5	6.2	1.7	1.6
1.6	6.0	15.4	6.6	1.5	1.1	6.2	22.5	7.1	1.0
1.3	2.7	6.3	3.0	1.7	1.6	1.7	7.1	1.9	1.7
1.0	1.4	1.5	1.7	1.4	1.4	1.6	1.0	1.7	1.5

Table 5.4: WFC Point Spread Functions.Shown as percentages (out of 100 percent) of the total flux in a 5 by 5 pixel region. On the left in each case is a model PSF with the observed wavefront errors and pixel response function. On the right is the diffraction limited case for comparison.

WFPC2 Model PSF			2000 Å: Peak near corner of WF pixel			Diffraction Limited PSF			
0.5	1.8	2.1	0.8	0.3	0.4	0.4	0.4	0.3	0.1
1.5	9.9	13.6	3.1	0.5	0.4	15.4	21.5	0.4	0.1
1.5	9.8	24.0	4.7	0.5	0.4	21.5	33.4	0.4	0.1
0.5	2.1	3.6	1.3	0.3	0.3	0.4	0.4	0.4	0.1
0.2	0.4	0.4	0.2	0.2	0.1	0.1	0.1	0.1	0.1
				Peak near center of pixel					
0.2	0.4	0.5	0.5	0.3	0.2	0.2	0.2	0.1	0.2
0.3	1.7	5.3	3.0	0.8	0.1	0.8	1.3	0.6	0.1
0.5	5.4	28.5	14.0	2.2	0.2	1.3	86.2	1.4	0.2
0.3	2.2	9.1	4.5	1.0	0.1	0.6	1.4	0.9	0.2
0.3	0.6	1.2	0.8	0.3	0.2	0.1	0.2	0.2	0.2
				4000 Å: Peak near corner of WF pixel					
0.8	2.6	2.5	0.8	0.2	0.4	0.5	0.5	0.2	0.1
2.6	16.1	16.4	3.0	0.4	0.5	17.7	21.2	0.6	0.1
2.0	12.9	17.3	3.0	0.4	0.5	21.2	26.7	0.6	0.1
0.6	2.0	2.6	0.9	0.2	0.2	0.6	0.6	0.4	0.2
0.2	0.4	0.3	0.2	0.1	0.1	0.1	0.1	0.2	0.2
				Peak near center of pixel					
0.3	0.6	0.7	0.5	0.3	0.3	0.2	0.3	0.2	0.2
0.6	3.1	7.2	3.4	0.7	0.2	0.7	3.7	0.7	0.2
0.9	8.5	33.3	10.2	1.2	0.3	3.7	68.8	5.3	0.4
0.4	2.5	8.8	3.0	0.6	0.2	0.7	5.3	0.8	0.2
0.2	0.5	0.9	0.5	0.3	0.2	0.2	0.4	0.2	0.3
				6000 Å: Peak near corner of WF pixel					
0.7	2.6	2.6	0.9	0.3	0.2	0.5	0.4	0.2	0.2
3.0	14.9	15.6	3.3	0.5	0.5	18.3	20.7	0.5	0.3
2.2	13.7	16.3	3.2	0.4	0.4	20.7	24.2	0.6	0.2
0.6	2.3	2.9	0.7	0.2	0.2	0.5	0.6	0.2	0.2
0.2	0.3	0.3	0.2	0.2	0.2	0.3	0.2	0.2	0.2
				Peak near center of pixel					
0.3	0.7	0.9	0.6	0.2	0.2	0.3	0.2	0.3	0.2
0.7	4.1	7.8	4.1	0.8	0.3	1.8	6.1	1.9	0.3
1.0	8.6	30.4	9.4	1.3	0.2	6.1	54.9	6.2	0.3
0.5	2.8	8.2	3.5	0.6	0.3	1.9	6.2	2.5	0.3
0.2	0.5	1.0	0.6	0.3	0.2	0.3	0.3	0.3	0.2
				8000 Å: Peak near corner of WF pixel					
1.0	3.0	2.9	1.1	0.3	0.1	2.0	2.0	0.2	0.2
3.6	13.1	13.6	4.0	0.5	2.0	15.8	17.3	2.2	0.1
2.6	12.6	14.2	3.5	0.5	2.0	17.3	19.3	2.5	0.1
0.8	3.2	3.6	1.0	0.3	0.2	2.2	2.5	0.2	0.2
0.2	0.4	0.5	0.2	0.1	0.2	0.1	0.1	0.2	0.1
				Peak near center of pixel					
0.2	0.8	0.8	0.7	0.3	0.1	0.2	0.3	0.2	0.1
0.9	4.6	6.9	4.4	1.0	0.2	3.5	4.6	3.4	0.2
0.9	7.5	30.8	8.1	1.2	0.3	4.6	52.0	5.0	0.3
0.5	3.1	7.3	3.7	0.7	0.1	3.4	5.1	3.9	0.2
0.2	0.5	1.0	0.7	0.2	0.1	0.2	0.3	0.2	0.1

5.6 PSF Variations with Field Position

The WFPC2 PSFs vary with field position due to field-dependent aberrations, obscuration shifting, and scattering. This will complicate photometry, PSF subtraction, and deconvolution (Krist, 1995).

The coma and astigmatism aberrations vary significantly within a camera across the field-of-view. These variations are simply part of the optical design. At the extreme corners of the WFC CCDs, away from the OTA axis, there is about 1/5 wave of astigmatism (referenced at 633 nm), which decreases to nearly zero at the CCD centers. Astigmatism at this level causes the PSF core to become elliptical and slightly less sharp; note flattening of PSF at pixels positions (54,777) and (605,148) in Figure 5.5. Coma also varies, but to a much lesser extent. Coma and astigmatism variations are considerably smaller in PC1.

Figure 5.5: PSF Variations with Field Position - Aberrations. Nine observed PSFs (filter F814W) are shown from a widely spaced grid on WF3. CCD pixel position are labeled. Note flattening of PSF in the (54,777) and (605,148) positions.

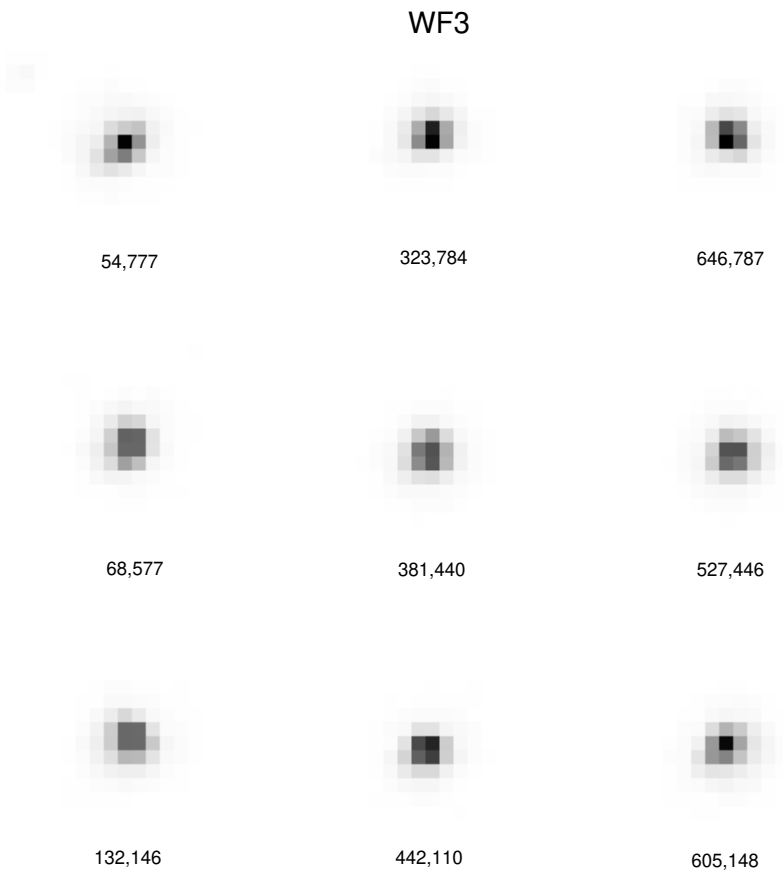

The obscuration patterns due to the camera optics (relay secondary mirror and spiders) appear to shift with respect to the OTA obscurations, depending on field position. The interacting diffraction patterns of the WFPC2 and OTA spiders cause ripples in the spider diffraction spikes, which vary with field position as the two spiders shift relative to each other. In Figure 5.6 the OTA spider is hidden behind the WFPC2 spider at the field center and hence the diffraction spikes there have a simple, smooth appearance (c.f. position 446,425). At the CCD corners, however, one or more vanes of the OTA spider moves out from behind the WFPC2 spider, and the double set of obscurations causes a "beating" pattern in the diffraction spikes.

The spiders also interact with light diffracted from zonal errors in the OTA mirrors, causing streaks in the scattering halo which vary in position and intensity.

Figure 5.6: PSF Variations with Field Position - Obscuration Shifts. Five saturated PSFs observed in F814W are shown from a widely spaced grid on WF4. Note changes in spider diffraction spikes. CCD pixel position are labeled.

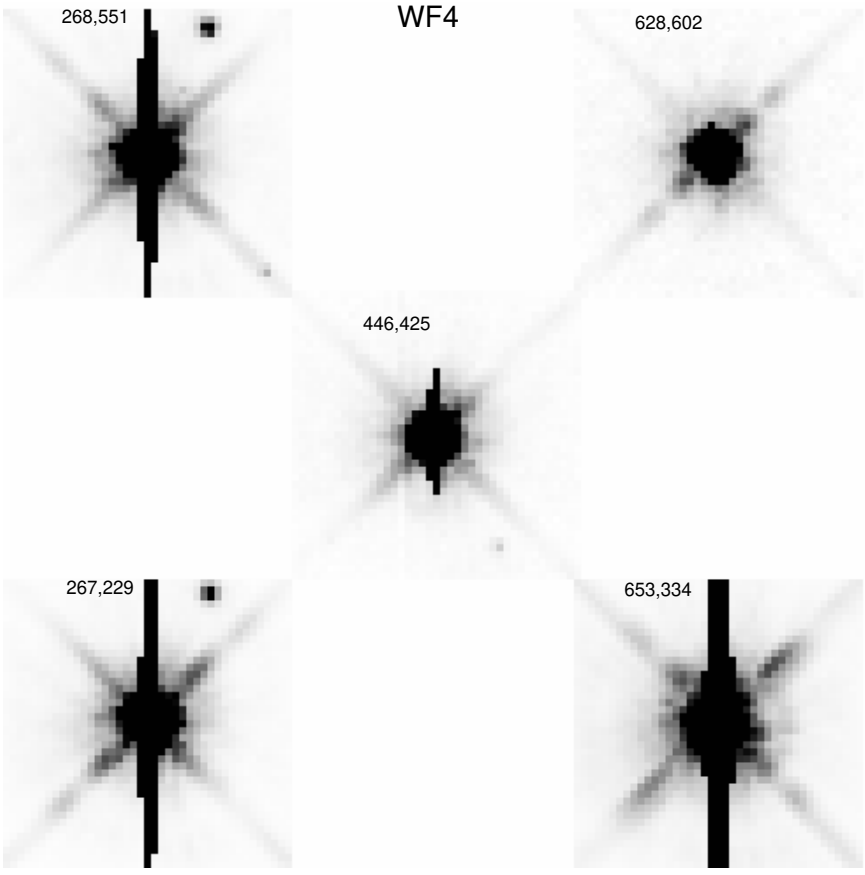

5.7 PSF Variations with Time

The shape and width of observed PSFs varies slightly over time, due to the change in focus of the telescope. The focus variation consists of two terms: a secular change, due to the ongoing shrinkage of the Metering Truss Assembly, at a currently estimated rate of 0.85 μm month^{-1}, and short-term variations, typically on an orbital time-scale (the so-called "breathing" of the telescope). The breathing is probably due to changes in the thermal environment as the telescope moves through its orbit, and has a typical peak-to-peak amplitude of 4 μm; larger variations are occasionally seen.

These small focus shifts will impact photometry performed with small (few pixel radius) apertures. Typical ±2μm focus shifts will result in photometric variations in the PC1 of 6.8%, 4.5%, 2.0%, and 0.2% for aperture radii of 1, 2, 3, and 5 pixels, respectively in F555W. This is based on the focus monitoring data taken over the period from July 1994 to January 1996 (Figure 5.7). Hence, "breathing" is often one of the major sources of errors for small-aperture photometry. However, relative photometry (i.e. the difference in magnitudes of stars in the same image) is not affected by this variation very much since all the stars in an image are impacted by the defocusing in a similar way. The variations are, of course, smaller for the WF chips because the pixels are roughly twice as large.

Figure 5.7: Measured OTA Focus Position (microns) as Function of Number of Days since January 1, 1994. Focus position is defined as difference between the optimal position of OTA secondary mirror and actual position, in microns.

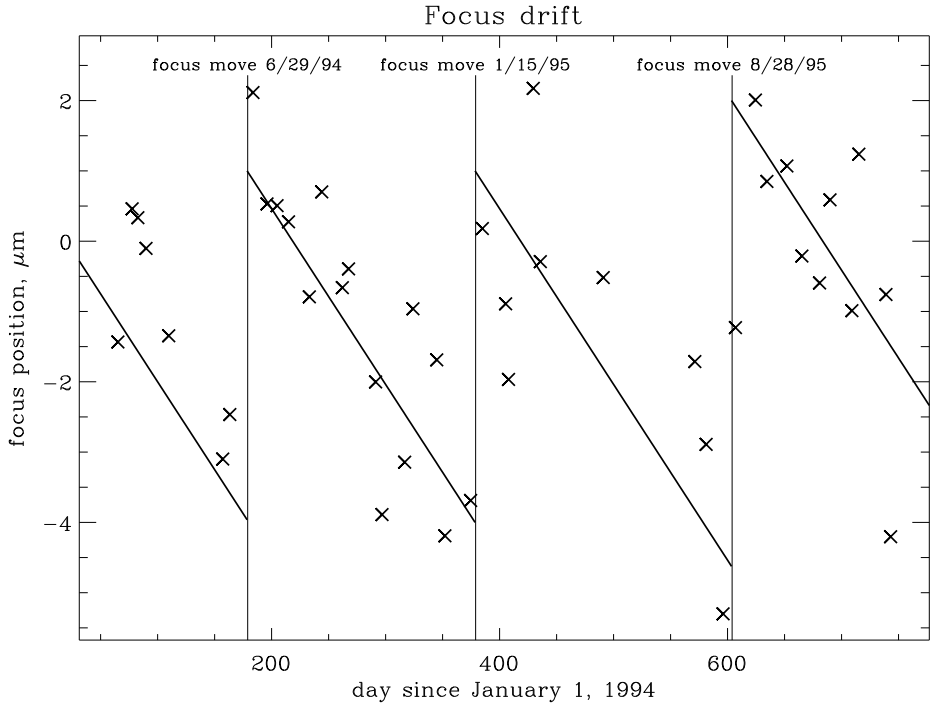

Figure 5.8: Measured Aperture Correction, V(r) - V(r=10 pix), in Magnitudes as Function of Shift from Optimal Focus. Data are given for aperture radii r=1, 2, 3, and 5 pixels for F555W filter on CCD PC1.

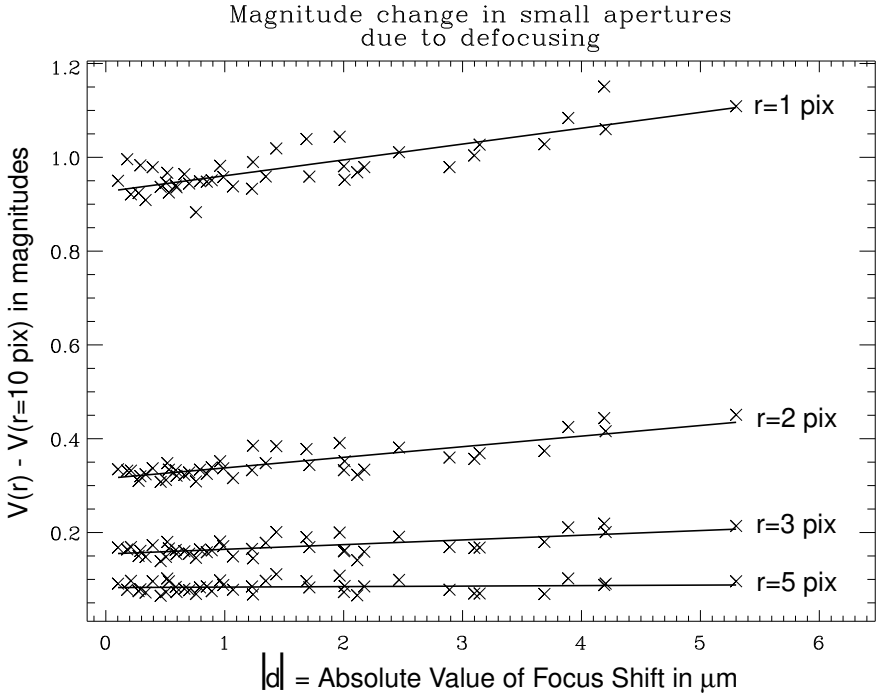

Systematic errors due to the secular focus drift can be corrected using the aperture corrections phased with the focus change (see Figure 5.8):

$$ap_corr = ap_corr_nominal + a(r) \times d$$

where ap_corr_nominal is the nominal aperture correction (mag) as derived from Table 2a in Holtzman et al. (1995a), a(r) is the flux variation per 1μm of focus drift (mag per micron) using an aperture with radius r (pixels), and d (μm) is the focus shift from the nominal position. The monitoring data mentioned above yield for PC1, F555W, the following values for a(r):

$$a(1\ pix) = 0.0338 \pm 0.0038$$

$$a(2\ pix) = 0.0226 \pm 0.0024$$

$$a(3\ pix) = 0.0100 \pm 0.0018$$

$$a(5\ pix) = 0.00105 \pm 0.0015$$

Values for other filters and other chips will be compiled in an instrument science report later in 1996.

Large focus changes, with amplitudes up to 10μm, are seen occasionally (See Hasan and Bely, Restoration of HST Images and Spectra II, p. 157). On May 1, 1994, and February 27, 1995, a short-lived defocusing of the telescope of up to 10μm was seen, probably due to extreme thermal conditions. Such a defocusing causes an increase of the PSF width by about 5-10% and a significant change in its

shape, especially evident in the PC both because of its higher resolution and its astigmatism (which makes the out-of-focus image appear elongated). The change in the PSF appears to be modeled adequately by the TIM software. (See Hasan and Bely, Restoration of HST Images and Spectra II, p. 157). (See sample PSF subtraction in Figure 7.2 on page 148).

5.8 Large Angle Scattering

Analysis of the WFPC2 saturated star images indicate that the large angle scattering (>3″ from a star) is significantly higher than expected.

Three data sets were used to determine the WFPC2 scattering. The first set was from the SMOV Ghost Check proposal 5615, in which 100 second images of δ Cas (V=2.7) were obtained at the center of each chip in F502N. The second set was a series of 6 second exposures of Vega (V=0.0) centered on WF2 through F410M (WFPC2 GTO proposal 5205). The third set was ε Eridani (V=3.73) centered on the PC and taken through F631N (500 sec each) and F953N (2200 sec each). These were from GTO proposal 5611.

WFPC2 scattering was determined by computing the azimuthal average and azimuthal median profiles. The regions near the diffraction spikes and saturated columns were not used. The profiles were determined using images corrected for horizontal smearing. After renormalizing to the XCAL fluxes the profiles agreed.

The measurements indicate that the average scatter in WFPC2 is an order of magnitude greater than in WF/PC- 1. The increase is due to scattering in WFPC2, not the OTA. In the WFPC2 images, the pyramid edge shadow is not visible in the scattered light; the light is spread out to the chip edges, indicating that most of the scattering occurs after the pyramid. However, the light level in adjacent channels is back down at the WF/PC-1 levels as shown in Figure 5.9.

The scattering does not show any strong dependence on wavelength between 410 nm and 953 nm, within the uncertainties of the measurements.

The scattered light is not uniform. There are high frequency spatial structures in the form of streaks radiating outwards from the star. These features are probably both wavelength and position dependent, and so cannot be readily subtracted.

The source of the WFPC2 scattering may be the CCDs. The WF/PC-l CCDs were back illuminated and had shiny surfaces. The electrode structure was not visible over most of the wavelength range. The WFPC2 CCDs, however, are front illuminated, so the electrode structure is visible and may be scattering the light. There was a large ghost in WF/PC-l due to a reflection between the CCD and filter, but no such feature has been seen in WFPC2. The flux from this missing ghost may instead constitute part of the scatter. (See also related material in “Observing Faint Targets Near Bright Objects” on page 146.)

Figure 5.9: Large Angle Scattering. The proportion of the total flux in F555W falling per square arcsecond as a function of the distance from the peak of a saturated stellar image. These curves are for a target in the PC. Note the large drop in the scattered light level when looking in an adjacent camera.

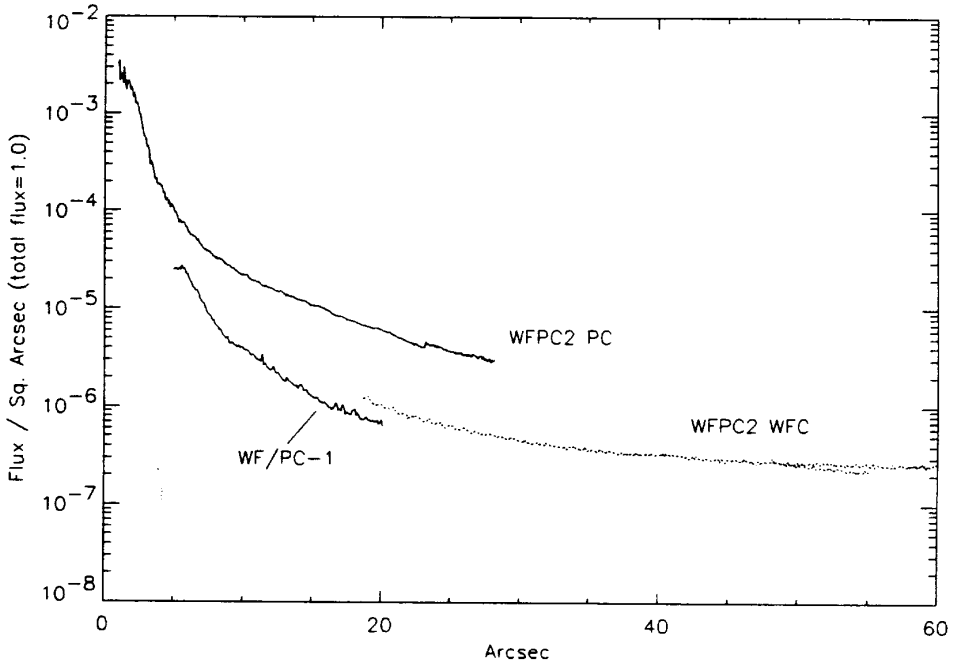

5.9 Ghost Images

Common ghost images result from internal reflections in the filters and in the field-flatteners. Two filter ghosts, caused by double (and quadruple) reflection inside the filter, are visible below and to the right of the star in Figure 5.10. The position and brightness of these ghosts varies from filter to filter, typically being most obvious in interference filters. The comatic shape of the ghost is caused by the camera optics being effectively misaligned for the light path followed by the ghost. The relative position of these ghosts does not vary much over the field.

An additional ghost is caused by an internal reflection inside the MgF_2 field flattener lens immediately in front of each CCD (Figure 5.11). The field flattener ghost is doughnut shaped (image of OTA pupil) in the WFC, but is smaller and more disk-like on the PC. This ghost contains ~0.15% of the total energy of the star. It is positioned on a line through the CCD center and the bright star; the distance from the ghost to the CCD center is 1.25 to 1.4 times the distance from

the bright star to the CCD center. This geometry results from curvature of the field flattener lens.

The large ghost image expected to be caused by reflection off the CCD back to the filter and then back to the CCD is not seen. It was deliberately eliminated in the PC by tilting the CCD slightly.

Figure 5.10: Saturated Stellar Image Showing Filter Ghosts. Intensity scale is logarithmic.

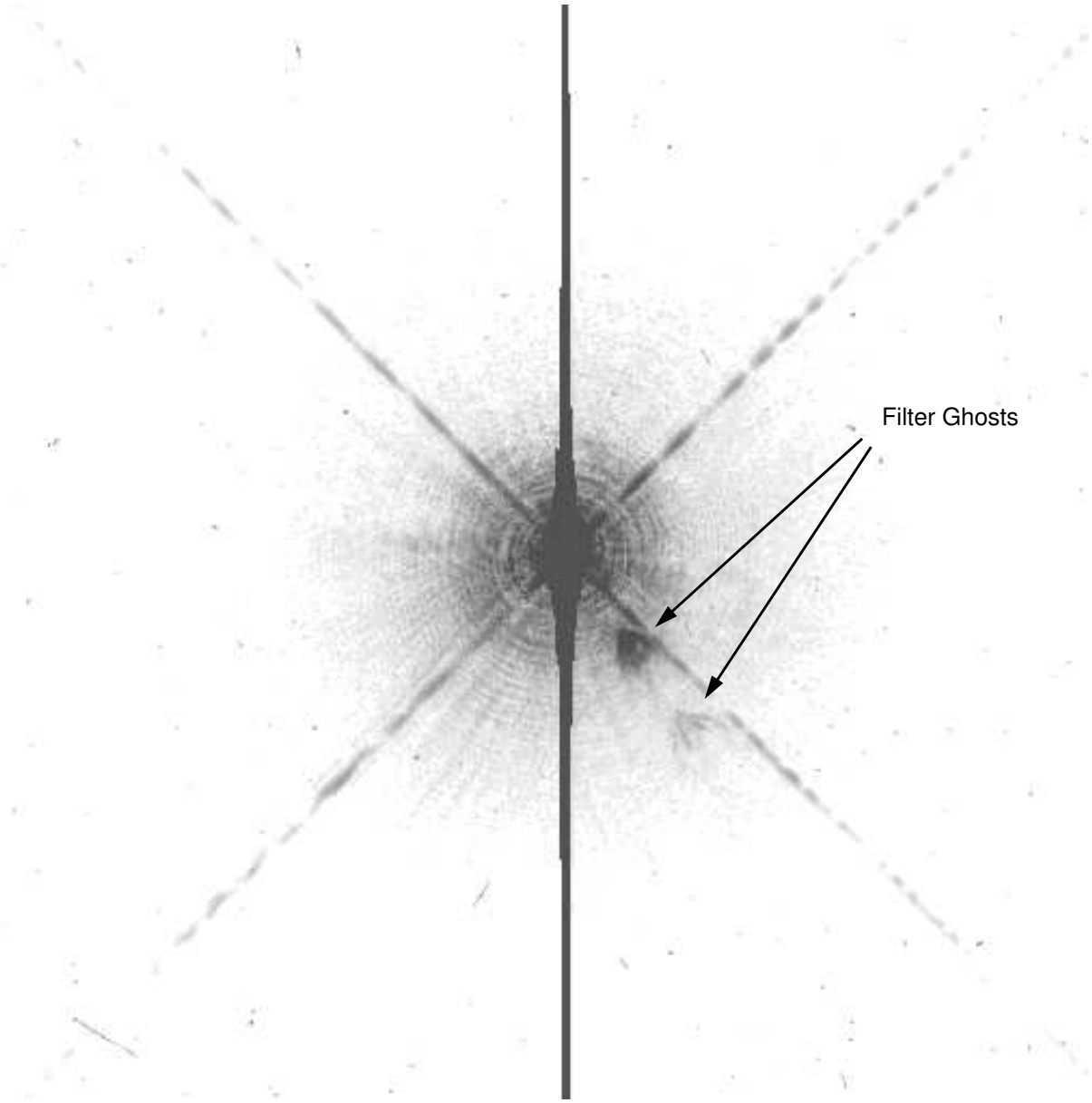

Figure 5.11: Saturated Stellar Image Showing Field Flattener Ghost on WF2.

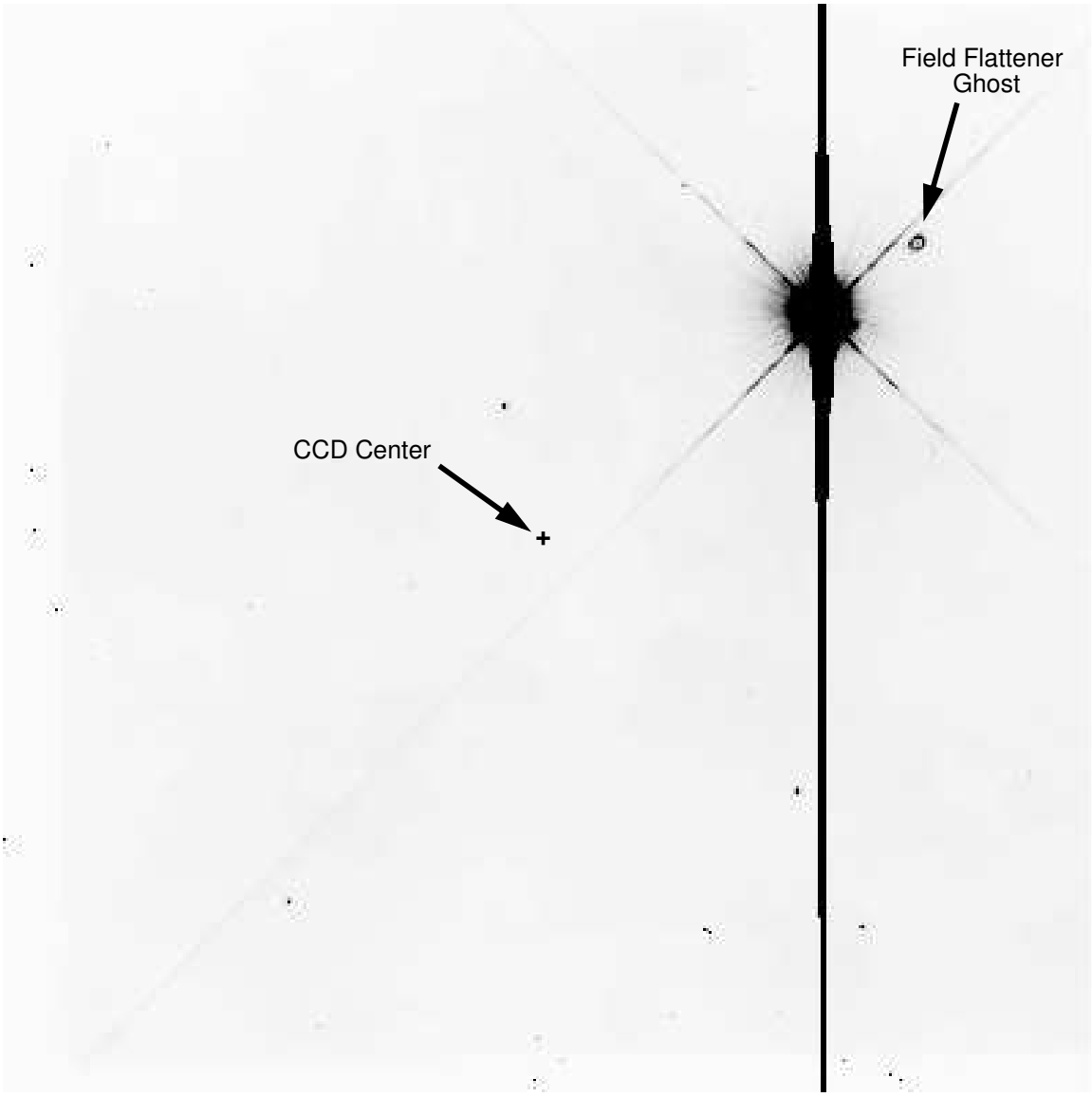

5.10 Optical Distortion

The WFPC2 cameras have significant geometric distortion which not only affects astrometry, but also affects photometry (because the extended sources used to generate flat fields have an induced change in apparent surface brightness). It can be a large effect, with "true" positions differing from observed positions by several pixels in the corners of the cameras. The distortion is wavelength dependent in the ultraviolet, because it is partially caused by the MgF_2 field flattener in front of each CCD. It is sensibly wavelength independent in the visible.

An estimate of the geometric distortion in the WFPC2 cameras was made (Holtzman et al., PASP 107, 156) from a series of 30 F555W exposures in a dense stellar field. Between each of these exposures, the telescope pointing was shifted by 16″ in a 6 x 5 grid along rows and columns. On any given frame, positions of several dozens of stars were measured. Any pair of stars which appeared on three or more of the 30 frames was used to do a cubic distortion solution. The cubic distortion coefficients are of the form:

$$x_{corr} = C_1 + C_2x + C_3y + C_4x^2 + C_5xy + C_6y^2 + C_7x^3 + C_8x^2y + C_9xy^2 + C_{10}y^3$$

$$y_{corr} = D_1 + D_2x + Dy + D_4x^2 + D_5xy + D_6y^2 + D_7x^3 + D_8x^2y + D_9xy^2 + D_{10}y^3$$

The coefficients are given in Table 5.5. The input (x,y) in the above equation are offsets from the center of each CCD in pixel units:

$$x = x_{obs} - 400$$

$$y = y_{obs} - 400$$

where (x_{obs}, y_{obs}) are the "observed" pixel positions on each CCD. The corrected values (x_{corr}, y_{corr}) are in a system with the origin near the pyramid apex, and the units are PC1 pixels. Hence PC1 in is quadrant 1, WF2 in quadrant 2, etc. Application of the transformation brings positions of all chips into the orientation of PC1.

The pixel scale can be estimated from the commanded offsets between the frames (relying on the FGS scale and distortion calibrations). It comes out as 0.04554 ± 0.00001 arcseconds pixel^{-1} in the PC, and hence 0.09961, 0.09958, and 0.09964 arcseconds pixel^{-1} in WF2, 3 and 4 respectively. An independent check on an astrometric standard field (M67) yielded 0.04555 arcseconds pixel^{-1} in the PC. These plate scales refer to the scale at the center of the chip in filter F555W. The true scale is lower elsewhere on the chip because of distortion, and there is some wavelength dependence in the scale even for visible wavelengths.

Table 5.5: Cubic Distortion Coefficients.

Coefficient	PC 1	WF2	WF3	WF4
C1	3.54356E+02	-8.12003E+02	-8.07068E+02	7.72904E+02
C2	1.00021 E+00	1.95172E-02	-2.18757E+00	1.37619E-02
C3	9.79758E-04	-2.18805E+00	-8.51284E-03	2.18899E+00
C4	9.84222E-08	-1.51015E-06	-3.21458E-07	1.33326E-06
C5	-6.31327E-09	5.06693E-06	2.77459E-06	-4.00828E-06
C6	-7.19983E-07	1.04063E-06	-2.06874E-06	-5.71282E-07
C7	-3.73922E-08	-4.55094E-10	7.39223E-08	-2.00520E-09
C8	6.65101E-10	7.50249E-08	-1.18833E-09	-7.86673E-08
C9	-3.51470E-08	-1.51652E-09	7.73056E-08	-3.37491E-09
C10	-2.55003E-09	7.34568E-08	-3.72971E-10	-7.81490E-08
D1	3.43646E+02	7.66592E+02	-7.71489E+02	-7.74638E+02
D2	1.00544E-03	2.18607E+00	7.40319E-03	-2.18688E+00
D3	9.99786E-01	2.02006E-02	-2.18554E+00	1.29831E-02
D4	-5.80870E-07	-3.79469E-06	-1.49841E-06	1.30814E-06
D5	-5.07221E-07	-2.99518E-06	2.96650E-06	2.01760E-06
D6	3.41574E-07	1.05789E-07	-2.02756E-07	-8.47656E-07
D7	-1.08091E-09	-7.47857E-08	-1.45720E-09	7.70408E-08
D8	-3.42070E-08	-1.67666E-09	7.72421E-08	-1.68514E-09
D9	1.17819E-09	-7.55302E-08	8.52633E-10	7.75257E-08

The cubic distortion coefficients can be used to derive effective pixel areas as presented in Figure 5.12. Contours are shown at half percent levels. Measurements of total brightness or total counts (as opposed to measurements of surface brightness) should be corrected by multiplying the science image by Figure 5.12. This correction image is also available in the HST data archive as file `f1k1552bu.r9h`.
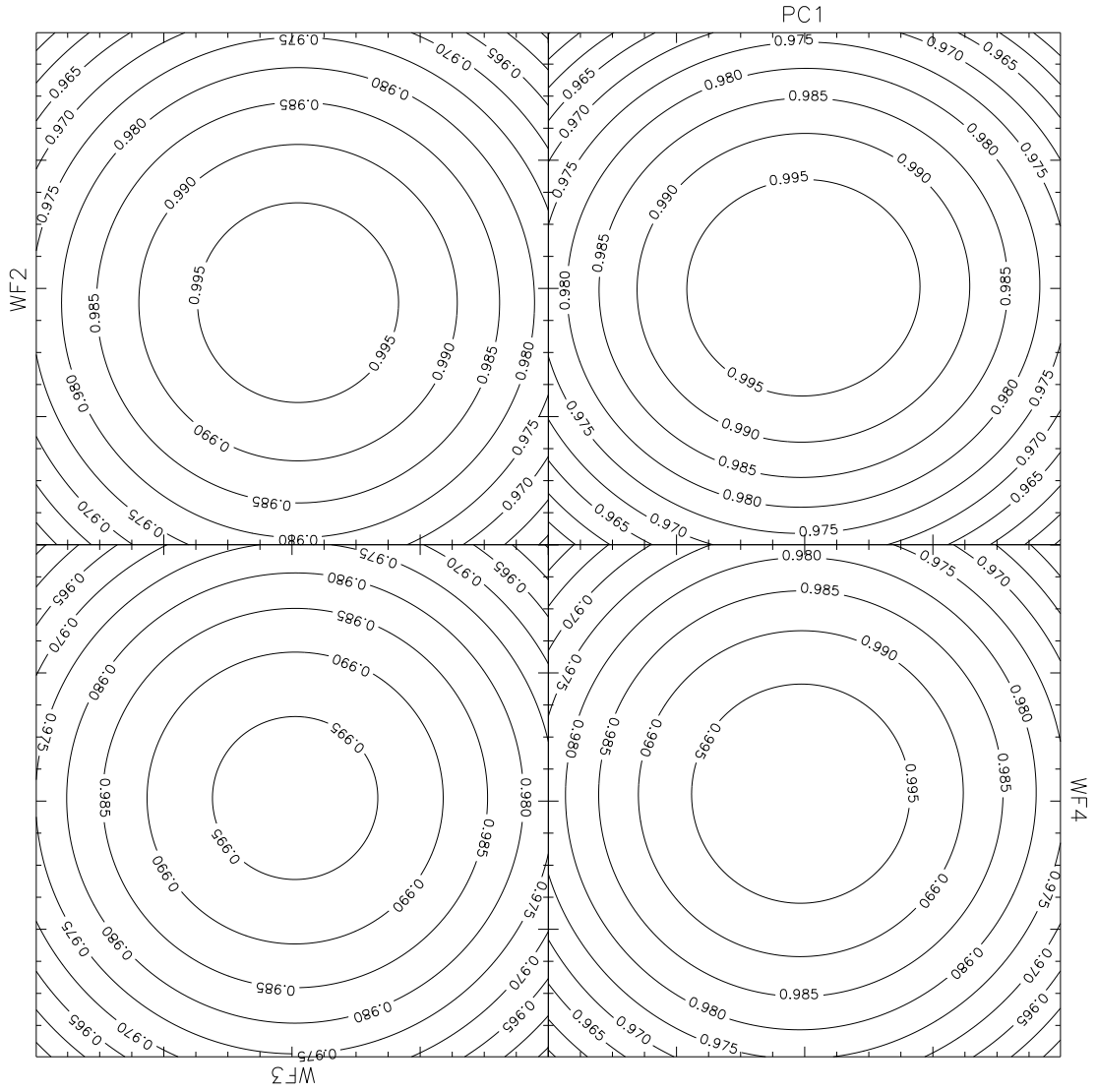
Figure 5.12: Integrated Photometry Correction Induced by Camera Distortions.